Tunable Room Temperature Magnetic Skyrmions in Ir/Fe/Co/Pt Multilayers

Anjan Soumyanarayanan,[1, 2, *] M. Raju,[2] A. L. Gonzalez Oyarce,[1] Anthony K. C. Tan,[2] Mi-Young Im,[3, 4]
A. P. Petrović,[2] Pin Ho,[1] K. H. Khoo,[5] M. Tran,[1] C. K. Gan,[5] F. Ernult,[1] and C. Panagopoulos[2, †]

[1]*Data Storage Institute, 2 Fusionopolis Way, 138634 Singapore*
[2]*Division of Physics and Applied Physics, School of Physical and Mathematical Sciences,*
Nanyang Technological University, 637371 Singapore
[3]*Center for X-ray Optics, Lawrence Berkeley National Laboratory, Berkeley, California 94720, USA*
[4]*Department of Emerging Materials Science, DGIST, Daegu 42988, Korea*
[5]*Institute of High Performance Computing, 1 Fusionopolis Way, 138632, Singapore*

Magnetic skyrmions are nanoscale topological spin structures offering great promise for next-generation information storage technologies. The recent discovery of sub-100 nm room temperature (RT) skyrmions in several multilayer films has triggered vigorous efforts to modulate their physical properties for their use in devices. Here we present a tunable RT skyrmion platform based on multilayer stacks of Ir/Fe/Co/Pt, which we study using X-ray microscopy, magnetic force microscopy and Hall transport techniques. By varying the ferromagnetic layer composition, we can tailor the magnetic interactions governing skyrmion properties, thereby tuning their thermodynamic stability parameter by an order of magnitude. The skyrmions exhibit a smooth crossover between isolated (metastable) and disordered lattice configurations across samples, while their size and density can be tuned by factors of 2 and 10 respectively. We thus establish a platform for investigating functional sub-50 nm RT skyrmions, pointing towards the development of skyrmion-based memory devices.

In conventional ferromagnets (FMs), the exchange interaction aligns spins, and the anisotropy determines energetically preferred orientations. Meanwhile, the Dzyaloshinskii-Moriya interaction[1,2] (DMI), generated by strong spin-orbit coupling (SOC) and broken inversion symmetry, induces a relative tilt between neighbouring spins. Magnetic skyrmions – finite-size two-dimensional (2D) 'whirls' of electron spin – form due to the competition between these 'winding' DMI and 'aligning' exchange interactions[3–7]. Skyrmions have several compelling attributes as prototype memory elements, namely their: (1) nontrivial spin topology, protecting them from disorder and thermal fluctuations[8–10], (2) small size and self-organization into dense lattices[5,6,11,12], and (3) solitonic nature, enabling particle-like dynamics, manipulation and addressability[10,12,13]. Originally magnetic skyrmions were discovered in non-centrosymmetric compounds hosting bulk DMI[4–7]. However, their emergence in thin multilayer films with interfacial DMI is particularly exciting[14,15] due to the inherent tunability of magnetic interactions in 2D, and the material compatibility with existing spintronic technology[8,16].

The DMI generated at interfaces between ultrathin FM layers and strong SOC metals[15,17–20] can host Néel-textured skyrmions – first observed in epitaxial monolayers of Fe on Ir(111)[11,12]. Whereas such ultrathin films can stabilize small skyrmions (∼8 nm) only at low temperatures (< 30 K), analogous multilayer films have recently been shown to host ∼50-100 nm RT skyrmions[21–23]. Here, a FM layer (e.g. Co) is sandwiched between different SOC metals (e.g. Pt and Ir/Ta) to produce a net effective DMI[21–23], and multiple repeats of such trilayers stabilize columnar skyrmions through interlayer exchange coupling[24,25]. Multilayer skyrmions have

been imaged using synchrotron-based microscopy techniques[21–23], with recent demonstrations of their confinement[21,23], nucleation and dynamics[22,26,27] in constricted geometries. To translate these attributes into functional RT devices, we must first develop methods of controlling and varying the physical properties of skyrmions, such as their thermodynamic stability, size and density.

Individual skyrmion addressability will be particularly important for technological applications. To realise this, we must achieve control over the skyrmion stability via the critical material parameter, κ[3,17,28–30]:

$$\kappa = \pi D / 4\sqrt{AK} \equiv D/D_{\rm c} , \qquad (1)$$

where A is exchange stiffness, D is the normalized DMI per unit area, and K is the out-of-plane anisotropy. For $\kappa > 1$, skyrmions are thermodynamically stable entities, forming a lattice at equilibrium, while for $0 < \kappa < 1$, they would be metastable, isolated particles[28–30]. It is also important to establish a route towards reducing the skyrmion size at RT to maximize its potential for energy-efficient, high-density memory. Furthermore, the ability to control skyrmion density would enable device performance tuning in both static[9] and dynamic[31,32] configurations. Investigating the technological relevance of multilayer skyrmions will also necessitate their electrical detection[33–35] and imaging[36] within stack configurations translatable to practical devices.

Here we describe our development of a new material platform – multilayer stacks of Ir/Fe/Co/Pt – as a host of sub-50 nm skyrmions with continuously tunable properties. By harnessing the large and opposite signs of DMI generated from Fe/Ir[11] and Co/Pt[20] interfaces, we achieve substantial control over the effective DMI governing skyrmion properties. We first

confirm the presence of nanoscale RT skyrmions via established X-ray microscopy techniques, and investigate their field evolution using magnetic force microscopy (MFM) and Hall transport. By varying FM layer composition and thickness, we control D, K and A, and thereby modulate the skyrmion stability parameter κ by an order of magnitude, the skyrmion size by a factor of 2, and the skyrmion density by a factor of 10. We thus establish a platform for realizing tunable, functional RT skyrmions in multilayers, and demonstrate how they may be studied using commonly available lab-based techniques.
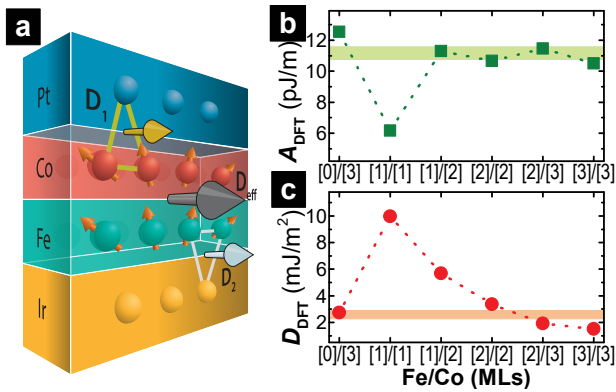
Multilayer Stack Structure

Fig. 1. **DMI Enhancement in Ir/Fe/Co/Pt Stacks.** (a) Schematic of our multilayer stack, featuring a sequence of Ir, Fe, Co, and Pt layers. The large DMI vectors at Co/Pt (top, $\vec{D}_1$) and Fe/Ir (bottom, $\vec{D}_2$) interfaces can act in concert to enhance the effective DMI, $\vec{D}_{\text{eff}}$. **(b-c)** DFT calculations of the exchange stiffness (A_{DFT}, b) and DMI (D_{DFT}, c) for Ir[3]/Fe[a]/Co[b]/Pt[3] stacks with varying Fe/Co composition (number of atomic layers in braces). The light green line in (b) indicates the typical magnitude of A_{DFT} for experimentally studied compositions. The addition of Fe leads to an enhancement of D_{DFT} relative to Fe[0]/Co[3], as shown by the light red line in (c).

The interfacial DMI is defined for neighbouring spins $\vec{S}_{1,2}$ as

$$\mathcal{H}_{\text{DMI}} = -\vec{D}_{12} \cdot (\vec{S}_1 \times \vec{S}_2) \qquad (2)$$

The magnitude and sign of $\vec{D}_{12}$, determined by the FM and SOC layers at the interface, govern the phenomenology of multilayer skyrmions[7,8]. Notably, the Co/Pt interface hosts a *large, positive DMI* ($d_{\text{Co-Pt}}^{\text{tot}} \sim +3$ meV)[20,23], enabling Co-based trilayers with large DMI (Co/Pt) and small DMI (e.g. Co/Ir[21], Co/MgO[23], Co/Ta[22] etc.) interfaces to host skyrmions. Meanwhile, the Fe/Ir interface hosts a *large, negative DMI* ($d_{\text{Fe-Ir}}^{\text{tot}} \sim -2$ meV)[11,19,20,37]. Therefore, a stack structure combining the Co/Pt and Fe/Ir interfaces, with large DMI of opposite signs, could exhibit additive enhancement of the effective DMI. Here we examine such a four-layer Ir/Fe/Co/Pt stack (Fig. 1a) and establish it as a platform for tailoring magnetic interactions and skyrmion properties.

To validate our hypothesis of DMI enhancement, we performed *ab initio* density functional theory (DFT) calculations of the magnetic interactions for the Ir/Fe/Co/Pt stack with varying Fe/Co composition. We determined the effective DMI, D_{DFT}, from the difference between the DFT calculated energies for clockwise and counter-clockwise chiral spin configurations, following the work of Yang *et al.*[20,23] (details in Methods, §S2). D_{DFT}, shown in Fig. 1c, has a prominent peak for Fe[1]/Co[1] (number of atomic layers in braces), supporting the hypothesis of DMI enhancement with the incorporation of an Fe layer. Importantly, for the same total FM thickness (e.g. Fe[1]/Co[2] c.f. Fe[0]/Co[3]), we obtain a substantial ($\sim 100\%$) DMI enhancement with Fe, which persists even for larger FM thicknesses (e.g. Fe[2]/Co[2]). During the preparation of this manuscript, we became aware of a similar result reported for one such composition (Fe[1]/Co[2])[38]. Meanwhile, the exchange stiffness, A_{DFT} (Fig. 1b), falls in a narrow range between 10.5-12.5 pJ/m for Fe/Co compositions corresponding to the experimental work. A notable exception to the trend is Fe[1]/Co[1] ($A_{\text{DFT}} \simeq 6.2$ pJ/m) – such lowering of A_{DFT} for magnetic monolayers is well documented[11,19,37]. Finally, increasing the Fe/Co ratio and the FM thickness would also result in reduced anisotropy[39]. Thus, varying the Fe/Co composition could enable the modulation of D, K, and A – thereby tailoring the ensuing skyrmion properties.

Multilayer films with [Ir(10)/Fe(x)/Co(y)/Pt(10)]$_{20}$ stacks (layer thickness in Å in parentheses) were sputtered on thermally oxidized Si wafers with optimized film texture and interface quality, and on Si$_3$N$_4$ membranes for X-ray microscopy (see Methods). The thickness of Fe (x : 0-6 Å) and Co (y : 4-6 Å) layers were varied across the films, and the samples studied are described in terms of their **Fe(x)/Co(y)** composition. While the results detailed here were measured in films with 20 stack repeats for enhanced X-ray contrast, similar trends were observed for transport and MFM in samples with 8 repeats. The data presented here were acquired following saturation at positive fields ($H > |H_S|$) in out-of-plane (OP) configuration. The OP magnetization ($M(H)$) loops for these stacks have a characteristic sheared shape (see e.g. Fig. 2j), which is typically a signature of labyrinth domain states[22].

Microscopic Imaging of RT Skyrmions

Fig. 2 shows representative images acquired by three different magnetic microscopy experiments in varying OP fields for sample **Fe(3)/Co(6)**. We begin by examining magnetic transmission soft X-ray microscopy (MTXM - a technique previously used to study multilayer skyrmion films[22]) images acquired using films grown on Si$_3$N$_4$ membranes (see Methods). Data recorded at the Co L$_3$ edge (778 eV) (Fig. 2a-c) show that as the field is reduced from $+H_S$, round-shaped sub-100 nm features with neg-
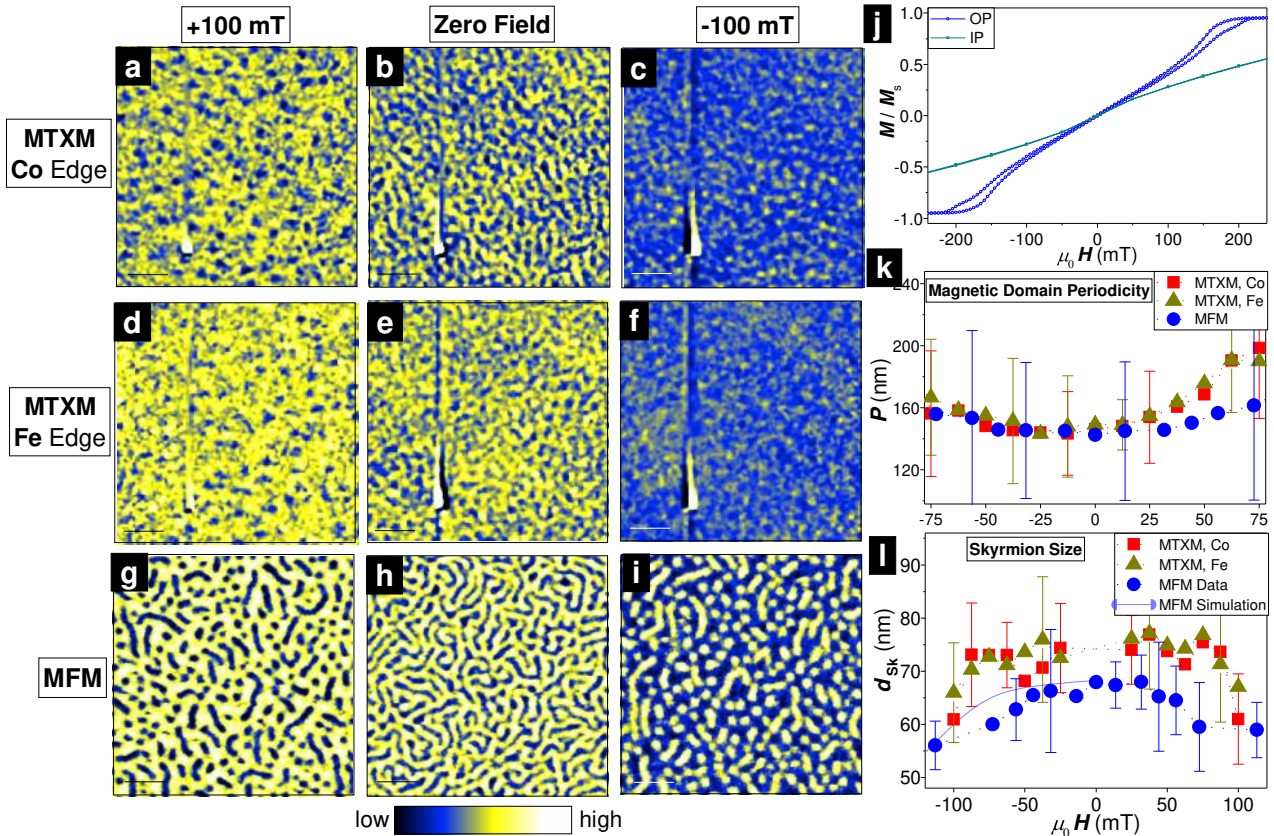
Fig. 2. **Magnetic Microscopy of RT Skyrmions. (a-i)** Microscopic imaging (scale bar: 0.5 μm) of sample **Fe(3)/Co(6)** at RT with MTXM (on Si_3N_4 membrane) at the Co L_3 edge (a-c), MTXM at the Fe L_3 edge (d-f), over the same sample region as (a-c), and with MFM (on SiO_2 substrate, g-i). Images shown are acquired at $\sim +100$ mT (a, d, g), 0 T (b, e, h) and ~ -100 mT (c, f, i) respectively after saturation at $\sim +250$ mT, and display similar evolution in magnetic contrast with applied field. A dead pixel on the MTXM CCD (a-f: bottom left) does not affect our analysis. **(j)** Hysteresis loops for out-of plane (OP, blue) and in-plane (IP, green) magnetization, M/M_S. **(k-l)** Comparisons of the field-dependent trends of magnetic domain periodicity, P (k) and the size of round features (skyrmions) d_{Sk} (l), measured in MTXM - Co (red), MTXM - Fe (green) and MFM (blue) experiments respectively. The size of Néel skyrmions that emerge in micromagnetic MFM simulations (thick blue line) is overlaid for comparison (simulation parameters for **Fe(3)/Co(6)** in Fig. 4d-f, details in methods). Representative error bars in (k) indicate the fit width of P, and in (l) the standard deviation of d_{Sk} across multiple (minimum 5) skyrmions respectively.

ative (blue) contrast emerge (Fig. 2a), which grow to form elongated labyrinthine domains at zero field (Fig. 2b). At negative fields, these domains give way to round-shaped features with positive (yellow) contrast (Fig. 2c), which shrink and disappear at $-H_S$. The sub-100 nm size and field evolution of these round magnetic features (Fig. 2l, data) show striking similarities to the emergence and evolution of Néel-textured magnetic skyrmions observed in micromagnetic simulations of these films (Fig. 2l, line: simulation parameters in Fig. 4d-f, details in Methods), and recently reported in similar multilayer films[21–23]. In contrast, we can rule out the presence of magnetic bubbles, which would be micron-sized and inherently unstable within our films (see Methods). Therefore, we can establish the identification of these round magnetic features as Néel skyrmions stabilized by interfacial DMI.

In contrast to known multilayer skyrmion hosts[21–23], Ir/Fe/Co/Pt stacks include an additional FM layer (Fe). This enables us to corroborate our observations by performing analogous MTXM experiments at the Fe L_3 edge (708 eV, Fig. 2d-f), over the same sample region as Fig. 2a-c. While the magnetic contrast is diminished (c.f. Fig. 2a-c), analogous magnetic textures persist with a comparable field evolution. Importantly, the measured magnetic domain periodicity and skyrmion size show excellent agreement across these two experiments (Fig. 2k-l), confirming that skyrmionic spin textures persist across the composite (Co/Fe) FM layer.

To facilitate direct comparison with electrical transport experiments, we also performed MFM measurements on similar stacks deposited on Si/SiO_2 wafers using high spatial resolution tips (diameter $\sim$30 nm, see Methods). The MFM results (Fig. 2g-i) show similar field evolution to MTXM – skyrmions at higher fields (Fig. 2g, i), and stripes at zero field (Fig. 2h) – while displaying markedly higher magnetic and spatial contrast. Despite the difference in substrates (Si/SiO_2 for MFM vs. Si_3N_4 membranes for MTXM), the MFM domain periodicity (Fig. 2k, blue) shows similar magnitude and field evolution trends as MTXM.
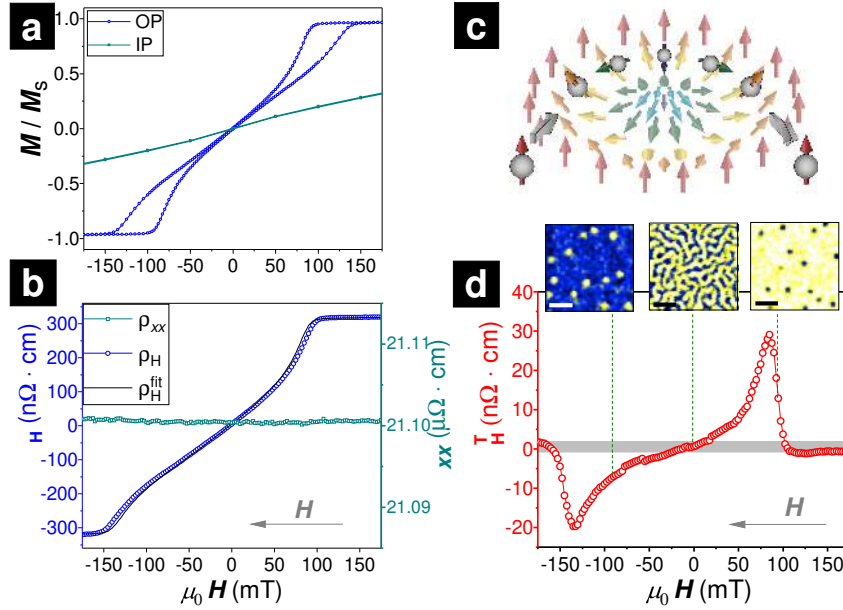
Fig. 3. **Topological Hall Effect (THE) from RT Skyrmions. (a)** OP (blue) and IP (green) magnetization, M/M_S, and **(b)** longitudinal (ρ_{xx}, green) and Hall (ρ_H, blue) resistivity as a function of applied field (grey arrow indicates sweep direction), for sample **Fe(2)/Co(6)** at RT. The black line (ρ_H^{fit}) is a fit to ρ_H, accounting for conventional and anomalous Hall effects (Eqn. 3[40]). **(c)** Schematic of adiabatic spin rotation of an itinerant electron (blue sphere, arrow indicates spin orientation) as it traverses the spin texture of a Néel skyrmion (spectral color scale shows OP magnetization component). The electron spin undergoes a 2π rotation, and the Berry phase accumulated results in the THE. **(d)** Residual Hall signal ρ_H^T, ascribed to THE from Néel skyrmions, obtained from (b) as $\rho_H^T(H) = \rho_H(H) - \rho_H^{\text{fit}}(H)$. Insets show MFM images (scale bar: 0.5 μm) acquired at fields corresponding to dashed green lines, indicating the magnetic structures that generate the THE signal.

Finally, we compare in Fig. 2l the field evolution of skyrmion size $d_{Sk}(H)$ as measured across all three experiments. The values of d_{Sk} reported in Fig. 2l correspond to measured values, and thus represent overestimates of the true skyrmion sizes to varying extents (due to differences in probe sizes and substrates). The MTXM results (red and green data) show good agreement between the Co and Fe experiments. Meanwhile, the MFM results (blue data) are in excellent correspondence with micromagnetic simulations (blue line), and also agree reasonably well with MTXM – albeit with a systematic offset of ~10 nm. Importantly, the excellent agreement between the d_{Sk} trends across experiments and simulations firmly establish MFM as a reliable tool for imaging RT skyrmions.

Hall Transport Experiments

To determine the electrical signature of Néel skyrmions, high-resolution magnetotransport measurements were performed on the films using small, non-perturbative current densities (as low as 10^4 A/m^2). Great care was taken to eliminate any field offsets between the transport data (Fig. 3b) and complementary magnetization measurements (Fig. 3a, see Methods). The typical RT transport characteristics for Ir/Fe/Co/Pt stacks (representative sample **Fe(2)/Co(6)**) are shown in Fig. 3b, with the longitudinal resistivity ($\rho_{xx}(H)$) constant to 0.02% within the field range of interest. The Hall resistivity data, $\rho_H(H)$ (Fig. 3b, blue), was analyzed by accounting for contributions from the conventional ($\propto H$)

and anomalous ($\propto M(H)$) Hall effects[40]:

$$\rho_H^{\text{fit}}(H) = R_0 \cdot H + R_S \cdot M(H) \qquad (3)$$

Here, R_0 is the conventional Hall coefficient, while R_S represents the cumulative anomalous Hall contribution from skew scattering, side-jump scattering, and the intrinsic (momentum space) Berry curvature mechanisms. After accounting for these contributions, a residual Hall signal, $\rho_H^T(H) = \rho_H(H) - \rho_H^{\text{fit}}(H)$, is observed with a maximum value of ~ 30 nΩ-cm (Fig. 3d) – the peak position consistent with an inflection in the raw ρ_H data (see §S3). Importantly, the field range corresponding to finite $\rho_H^T(H)$ is in good agreement with that over which skyrmions are observed in MFM (Fig. 3d insets) and MTXM experiments. We note that in bulk DMI materials, the observed $\rho_H^T(H)$ (5-100 nΩ-cm) has been attributed to Bloch skyrmions[33,35,41]. Based on the field range, consistency and reproducibility of $\rho_H^T(H)$ across samples (§S3), we ascribe its origin to the topological Hall effect (THE) from Néel skyrmions.

The THE results from the Berry phase accumulated by itinerant electrons crossing the 2D skyrmion spin texture (Fig. 3c). The $\rho_H^T(H)$ profile has a characteristic hump shape – weak at low field due to the predominance of 1D stripes (Fig. 3d, centre inset), with a peak at higher field due to skyrmion proliferation (Fig. 3d, left/right insets), which disappears at saturation[33,35,42]. One key contrast with $\rho_H^T(H)$ in Bloch skyrmion materials[35,41] is the observed asymmetry through the field sweep: in our

case $\left|\rho_{\mathrm{H}}^{\mathrm{T}}(+H)\right| \neq \left|\rho_{\mathrm{H}}^{\mathrm{T}}(-H)\right|$. Such asymmetry is likely due to hysteretic domain formation driven by the interfacial anisotropy in our multilayers. Second a direct comparison between the magnitude of $\rho_{\mathrm{H}}^{\mathrm{T}}(H)$ and the observed skyrmion density in MFM images gives an emergent flux per skyrmion of $6 - 100\,\phi_0$ across our multilayers ($\phi_0 = h/e$ is the flux quantum, procedural details in §S3). Such a large emergent flux is in contrast to corresponding reports on Bloch materials ($\mathcal{O}(1) \cdot \phi_0$[33,35,41]). This quantitative discrepancy could be addressed in future by a systematic comparison between Hall transport and observed magnetic textures. We note that this is the first reported electrical signature of RT skyrmions, establishing the utility of Hall transport towards skyrmion detection in RT devices.
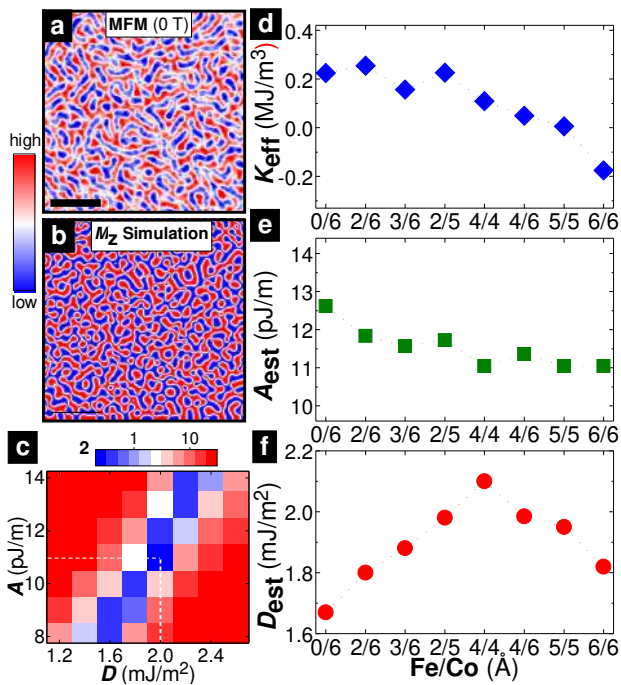
Modulating Magnetic Interactions

Fig. 4. **Modulating Magnetic Interactions with Fe/Co Composition. (a-b)** MFM image (a) and best-fit micromagnetic simulation (M_z, b) (scale bar: 0.5 μm) of the zero field magnetic contrast for sample **Fe(4)/Co(6)**. **(c)** A χ^2-fit comparison of the magnetic domain periodicity between MFM data (a) and micromagnetic simulations, with parameters A and D varied over a range of likely values. The best fit for **Fe(4)/Co(6)** corresponds to $A_{\mathrm{est}} = 11.4$ pJ/m, $D_{\mathrm{est}} = 2.0$ mJ/m^2 (dashed white lines, details in methods). **(d-f)** The variation of magnetic interactions K_{eff} (d), A_{est} (e), and D_{est} (f, obtained using c) across the samples studied in this work. D_{est} is found to be largest for **Fe(4)/Co(4)**, at (2.1 ± 0.2) mJ/m^2.

Having confirmed the presence of RT skyrmions, we examine the effects of varying **Fe(x)/Co(y)** composition on the magnetic interactions governing skyrmion properties. First, K_{eff} was determined directly from magnetization measurements, and was found to decrease with increasing Fe/Co ratio and FM thickness (Fig. 4d). Next, the exchange stiffness, A_{est} was estimated from DFT calculations (see Methods), and

is expected to vary by $\sim 15\%$ (11.0 - 12.6 pJ/m) over the Fe/Co compositions studied (Fig. 4e). The corresponding DMI, D_{est}, was determined by comparing the zero field magnetic domain periodicity in MFM experiments (Fig. 4a, for **Fe(4)/Co(6)**) with corresponding micromagnetic simulations (Fig. 4b, see Methods)[21,22] using a 2D χ^2 fit, with D and A varied over a range of likely values (Fig. 4c). Subsequently, the validity of D_{est} and A_{est} was established by independently performing χ^2-fits to the field-dependent ssssskyrmion size, $d_{\mathrm{Sk}}^{\mathrm{MFM}}(H)$, between experiments and simulations with varying D and A (see §S4). Notably, D_{est} showed a systematic 'dome'-like variation of $\sim 30\%$ across samples, ranging from $1.65 - 2.1$ mJ/m^2 (Fig. 4f) – the maximal value being larger than previous reports for other multilayer skyrmion hosts[21–23].

The DMI enhancement observed for Fe($x > 0$) relative to **Fe(0)/Co(6)** (Ir/Co/Pt) is consistent with DFT calculations (Fig. 1c). The inclusion of Fe results in the gradual formation of a Fe/Ir interface and corresponding suppression of the Co/Ir boundary, leading to increasing DMI. The DMI reaches its maximal value for complete monolayer coverage at both Fe/Ir and Co/Pt interfaces (near **Fe(4)/Co(4)**), and reduces as the FM layer thickness is further increased due to its interfacial nature. Notably, the 'dome'-like variation in D_{est} (Fig. 4f) does not track the decreasing trend of K_{eff} (Fig. 4d) or that of A_{est} (Fig. 4e). This indicates that a degree of independent variation of $(D/A)_{\mathrm{est}}$ and K_{eff} can be achieved within our samples.

Tuning Skyrmion Properties

The observed variation of D_{est}, K_{eff}, and A_{est} has direct implications on the properties of skyrmions, whose stability, size and density evolve visibly across our sample compositions (Fig. 5b-e). First, the stability parameter, κ_{est} ($\equiv D_{\mathrm{est}}/D_{\mathrm{c}}$, Eqn. 1) varies smoothly from ~ 0.8 to ~ 6.5 (Fig. 5a). This order of magnitude variation has a dramatic effect on the spatial configurations of skyrmions near maximal density ($H \sim -0.8\,H_S$) (Fig. 5b-e). The skyrmion configurations can be analyzed using Delaunay triangulation statistics (details in §S5) for the nearest neighbor (NN) coordination number (N_{NN}, Fig. 5f) and angular orientation (θ_{NN}, Fig. 5g)[43]. For $\kappa_{\mathrm{est}} < 1$ (Fig. 5f-g, bottom plots), the distributions show a large spread, with a marked deviation from ordered configurations, and correspond to metastable, isolated skyrmions (circular FT, Fig. 5c inset). In contrast, for $\kappa_{\mathrm{est}} > 1$, the distributions gradually converge around $N_{\mathrm{NN}} = 6$, $\theta_{\mathrm{NN}} = 60°$ – forming a disordered hexagonal skyrmion lattice (Fig. 5e inset). The crossover between isolated and lattice configurations appears to be smooth, possibly due to the granularity of magnetic properties and disorder pinning effects in sputtered films. Such a gradual crossover would likely enable skyrmion stabilization over a wide range of sizes and densities,
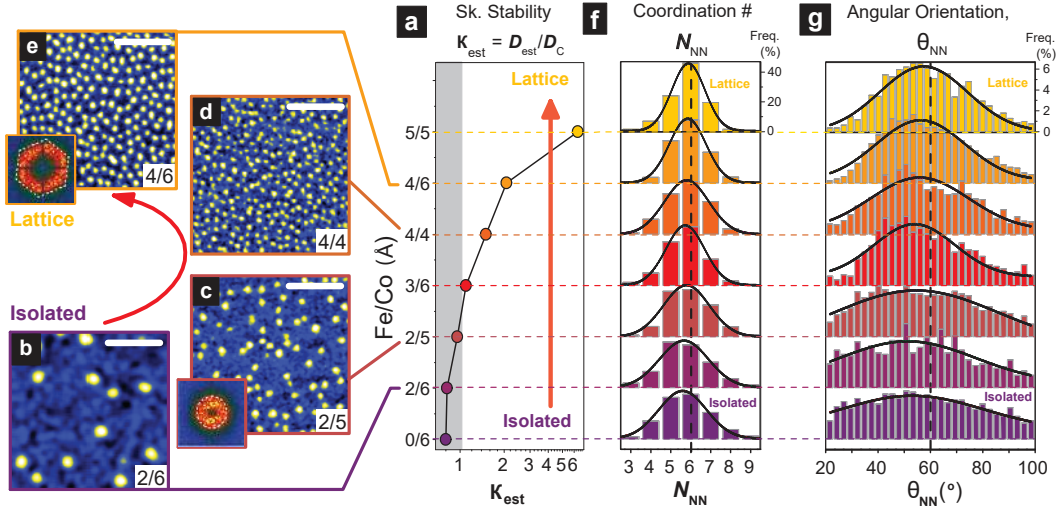
Fig. 5. **Tuning Skyrmion Stability with Fe/Co Composition. (a)** Evolution of the stability parameter $\kappa_{est} \equiv D_{est}/D_c$ from $\sim 0.8 - 6.5$ across our samples. **(b-e)** MFM images (scale bar: 0.5 μm) of skyrmion configurations at $H \sim -0.8\,H_S$ (max. density), for samples **Fe(2)/Co(6)** (b), **Fe(2)/Co(5)** (c), **Fe(4)/Co(4)** (d), and **Fe(4)/Co(6)** (e) respectively. With increasing κ, the configuration evolves from sparse, isolated particles (b) to a dense, disordered lattice (e), with visible variations in skyrmion size. The short-range hexagonal order in (e) is evident from the hexagonal Fourier transform (FT, inset), in contrast to the circular FT for (c) (inset). **(f-g)** Quantitative analysis of skyrmion configuration across samples, using Delaunay triangulation (details in §S5) to determine nearest neighbor (NN) statistics (min. sample size: 150 skyrmions): (f) NN coordination number, N_{NN}, and (g) NN angular orientation, θ_{NN}. With increasing κ, the distributions converge around $N_{NN} = 6$ and $\theta_{NN} = 60°$ (hexagonal lattice).

while maintaining individual addressability.
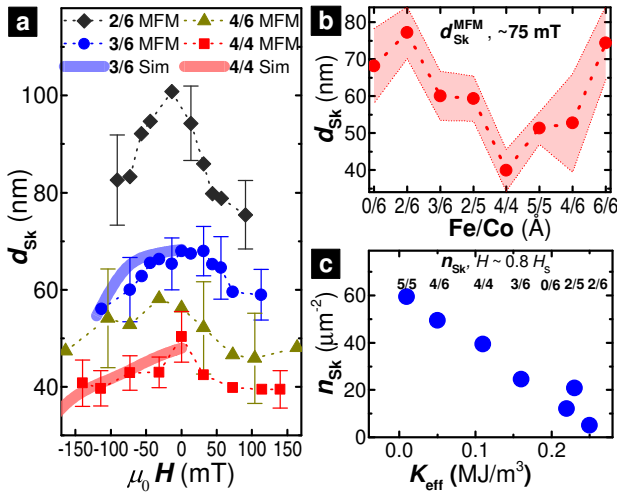

Fig. 6. **Tuning Skyrmion Properties with Fe/Co Composition. (a)** Field dependence of the skyrmion size, d_{Sk}^{MFM}, measured in MFM images for samples **Fe(2)/Co(6)** (black), **Fe(3)/Co(6)** (blue), **Fe(4)/Co(6)** (green), and **Fe(4)/Co(4)** (red). The MFM results in are compared with corresponding micromagnetic MFM simulations (parameters from Fig. 4d-f) for **Fe(3)/Co(6)** (blue line) and **Fe(4)/Co(4)** (red line) respectively. **(b)** Variation of d_{Sk}^{MFM} across samples at $\mu_0 H \simeq 75$ mT (shaded red region indicates error bars), showing a prominent dip for **Fe(4)/Co(4)** and a visible anti-correlation with D_{est} (Fig. 4f). Error bars for (a-b) indicate the standard deviation of d_{Sk} across multiple (minimum 5) skyrmions. **(c)** Variation of skyrmion density, n_{Sk} with K_{eff}, as measured across samples at $H \simeq 0.8\,H_S$. Corresponding Fe/Co compositions are indicated at the top.

Fig. 6a details the field dependence of the MFM skyrmion size, d_{Sk}^{MFM}, for four representative sam-

ples. Notably, skyrmions in **Fe(4)/Co(4)** ($(D/A)_{est} \simeq 0.19$: $d_{Sk}^{MFM} < 40$ nm) are considerably smaller than in **Fe(2)/Co(6)** ($(D/A)_{est} \simeq 0.14$), **Fe(3)/Co(6)** ($(D/A)_{est} \simeq 0.16$), and **Fe(4)/Co(6)** ($(D/A)_{est} \simeq 0.17$). The enhancement of DMI in **Fe(4)/Co(4)** likely induces a faster spatial spin rotation, resulting in a large ($> 2\times$) reduction in skyrmion size c.f. **Fe(2)/Co(6)**. The influence of DMI on skyrmion size is further evident from the trend in d_{Sk}^{MFM} across all our samples (Fig. 6b), which shows a prominent minimum at **Fe(4)/Co(4)**, and visible anti-correlation with the 'dome'-shaped variation in DMI (Fig. 4f). Notably, the excellent agreement in $d_{Sk}(H)$ trends between the MFM data and corresponding micromagnetic simulations (Fig. 6a) underscores the direct relationship between varying magnetic interactions and skyrmion properties across Fe/Co compositions. Finally, we note that the d_{Sk}^{MFM} values reported here overestimate the true skyrmion size, due to finite size probe convolution effects ($\sim$30 nm MFM tips). In fact, RT skyrmions in **Fe(4)/Co(4)** could be considerably smaller than any multilayer skyrmions reported so far[21-23] (see §S4).

While D/A plays a key role in determining the skyrmion size, the variation in K_{eff} is understood to govern the skyrmion density n_{Sk}. Fig. 6c shows the variation in n_{Sk} (for $H \sim 0.8\,H_S$), as a function of K_{eff} across our samples. As K_{eff} is reduced from strongly OP ($\sim$0.3 MJ/m^3) to near-IP (~ 0.01 MJ/m^3), n_{Sk} shows a dramatic increase: from ~ 5 μm^{-2} to ~ 60 μm^{-2}. Skyrmions in low K_{eff} samples are stable over a broader range of fields ($> \pm0.2$ T), due to increased H_S, and are also nucleated close to zero field with much greater ease. Therefore, varying K_{eff} on ei-

ther side of the optimal DMI composition is a route towards engineering stacks with the requisite skyrmion density and stability for specific applications.

Outlook

We have synthesized magnetic multilayer stacks hosting RT skyrmions with tunable properties. By varying the Fe/Co composition, we have modulated the magnetic interactions governing skyrmion formation, thereby continuously tuning the thermodynamic stability parameter, κ_{est}, over an order of magnitude. The resulting skyrmion configuration, imaged by X-ray microscopy and MFM, evolves from isolated, metastable particles to a disordered hexagonal lattice. Modulating D, K and A further enables us to vary the skyrmion size (by 2×) and density (by 10×). This demonstration of a platform for tunable sub-50 nm RT skyrmions and their electrical detection via Hall transport has immediate relevance for device applications.

The myriad proposals of skyrmion-based memory devices predominantly build upon either (a) the nucleation or deletion of single skyrmions in nanostructures[8,9,29], or (b) the dynamics of a train of skyrmions in a racetrack configuration[31,44,45]. The material requirements for (a) would be geared towards the use of individual, isolated skyrmions in confined geometries. In contrast, optimal materials for devices based on (b) would correspond to dense arrays of skyrmions, ideally in an ordered configuration, for high-speed readout and increased mobility. As demonstrated here, Ir/Fe/Co/Pt stacks can directly address both these contrasting requirements of skyrmion properties by simply varying the stack composition. Crucially, the smooth crossover between isolated and lattice configurations with composition can simultaneously enable stabilization and individual addressability for a wide range of skyrmion sizes and densities. We thus provide a material platform for fast-tracking technological explorations of skyrmion-based memory devices.

---

[*] souma@dsi.a-star.edu.sg
[†] christos@ntu.edu.sg

[1] Dzyaloshinsky, I. A thermodynamic theory of weak ferromagnetism of antiferromagnetics. *Journal of Physics and Chemistry of Solids* **4**, 241–255 (1958).

[2] Moriya, T. Anisotropic Superexchange Interaction and Weak Ferromagnetism. *Physical Review* **120**, 91–98 (1960).

[3] Bogdanov, A. & Hubert, A. Thermodynamically stable magnetic vortex states in magnetic crystals. *Journal of Magnetism and Magnetic Materials* **138**, 255–269 (1994).

[4] Rößler, U. K., Bogdanov, A. N. & Pfleiderer, C. Spontaneous skyrmion ground states in magnetic metals. *Nature* **442**, 797–801 (2006).

[5] Mühlbauer, S. *et al.* Skyrmion lattice in a chiral magnet. *Science* **323**, 915–919 (2009).

[6] Yu, X.-Z. *et al.* Real-space observation of a two-dimensional skyrmion crystal. *Nature* **465**, 901–904 (2010).

[7] Nagaosa, N. & Tokura, Y. Topological properties and dynamics of magnetic skyrmions. *Nature Nanotechnology* **8**, 899–911 (2013).

[8] Fert, A., Cros, V. & Sampaio, J. Skyrmions on the track. *Nature Nanotechnology* **8**, 152–156 (2013).

[9] Sampaio, J., Cros, V., Rohart, S., Thiaville, A. & Fert, A. Nucleation, stability and current-induced motion of isolated magnetic skyrmions in nanostructures. *Nature Nanotechnology* **8**, 839–844 (2013).

[10] Hagemeister, J., Romming, N., von Bergmann, K., Vedmedenko, E. Y. & Wiesendanger, R. Stability of single skyrmionic bits. *Nature Communications* **6**, 8455 (2015).

[11] Heinze, S. *et al.* Spontaneous atomic-scale magnetic skyrmion lattice in two dimensions. *Nature Physics* **7**, 713–718 (2011).

[12] Romming, N. *et al.* Writing and Deleting Single Magnetic Skyrmions. *Science* **341**, 636–639 (2013).

[13] Schulz, T. *et al.* Emergent electrodynamics of skyrmions in a chiral magnet. *Nature Physics* **8**, 301–304 (2012).

[14] Fert, A. Magnetic and Transport Properties of Metallic Multilayers. *Materials Science Forum* **59-60**, 439–480 (1990).

[15] Bode, M. *et al.* Chiral magnetic order at surfaces driven by inversion asymmetry. *Nature* **447**, 190–193 (2007).

[16] Soumyanarayanan, A., Reyren, N., Fert, A. & Panagopoulos, C. Emergent phenomena induced by spin-orbit coupling at surfaces and interfaces. *Nature* **539**, 509–517 (2016).

[17] Heide, M., Bihlmayer, G. & Blügel, S. Dzyaloshinskii-Moriya interaction accounting for the orientation of magnetic domains in ultrathin films: Fe/W(110). *Physical Review B* **78**, 140403 (2008).

[18] Cho, J. *et al.* Thickness dependence of the interfacial Dzyaloshinskii-Moriya interaction in inversion symmetry broken systems. *Nature Communications* **6**, 7635 (2015).

[19] Dupé, B., Hoffmann, M., Paillard, C. & Heinze, S. Tailoring magnetic skyrmions in ultra-thin transition metal films. *Nature Communications* **5**, 4030 (2014).

[20] Yang, H., Thiaville, A., Rohart, S., Fert, A. & Chshiev, M. Anatomy of Dzyaloshinskii-Moriya Interaction at Co/Pt Interfaces. *Physical Review Letters* **115**, 267210 (2015).

[21] Moreau-Luchaire, C. *et al.* Additive interfacial chiral interaction in multilayers for stabilization of small individual skyrmions at room temperature. *Nature Nanotechnology* **11**, 444–448 (2016).

[22] Woo, S. *et al.* Observation of room-temperature magnetic skyrmions and their current-driven dynamics in ultrathin metallic ferromagnets. *Nature Materials* **15**, 501–506 (2016).

[23] Boulle, O. *et al.* Room-temperature chiral magnetic skyrmions in ultrathin magnetic nanostructures. *Nature Nanotechnology* **11**, 449–454 (2016).

[24] Chen, G., Mascaraque, A., N'Diaye, A. T. & Schmid, A. K. Room temperature skyrmion ground state stabilized through interlayer exchange coupling. *Applied Physics Letters* **106**, 242404 (2015).

[25] Nandy, A. K., Kiselev, N. S. & Blügel, S. Interlayer Exchange Coupling: A General Scheme Turn-

ing Chiral Magnets into Magnetic Multilayers Carrying Atomic-Scale Skyrmions. *Physical Review Letters* **116**, 177202 (2016).

[26] Jiang, W. *et al.* Blowing magnetic skyrmion bubbles. *Science* **349**, 283–286 (2015).

[27] Büttner, F. *et al.* Dynamics and inertia of skyrmionic spin structures. *Nature Physics* **11**, 225–228 (2015).

[28] Kiselev, N. S., Bogdanov, A. N., Schäfer, R. & Rößler, U. K. Chiral skyrmions in thin magnetic films: new objects for magnetic storage technologies? *Journal of Physics D: Applied Physics* **44**, 392001 (2011).

[29] Rohart, S. & Thiaville, A. Skyrmion confinement in ultrathin film nanostructures in the presence of Dzyaloshinskii-Moriya interaction. *Physical Review B* **88**, 184422 (2013).

[30] Leonov, A. O. *et al.* The properties of isolated chiral skyrmions in thin magnetic films. *New Journal of Physics* **18**, 065003 (2016).

[31] Tomasello, R. *et al.* A strategy for the design of skyrmion racetrack memories. *Scientific Reports* **4**, 6784 (2014).

[32] Zhang, X., Zhou, Y., Ezawa, M., Zhao, G. P. & Zhao, W. Magnetic skyrmion transistor: skyrmion motion in a voltage-gated nanotrack. *Scientific Reports* **5**, 11369 (2015).

[33] Neubauer, A. *et al.* Topological Hall Effect in the *A* Phase of MnSi. *Physical Review Letters* **102**, 186602 (2009).

[34] Raičević, I. *et al.* Skyrmions in a Doped Antiferromagnet. *Physical Review Letters* **106**, 227206 (2011).

[35] Porter, N. A., Gartside, J. C. & Marrows, C. H. Scattering mechanisms in textured FeGe thin films: Magnetoresistance and the anomalous Hall effect. *Physical Review B* **90**, 024403 (2014).

[36] Milde, P. *et al.* Unwinding of a Skyrmion Lattice by Magnetic Monopoles. *Science* **340**, 1076–1080 (2013).

[37] Dupé, B., Bihlmayer, G., Böttcher, M., Blügel, S. & Heinze, S. Engineering skyrmions in transition-metal multilayers for spintronics. *Nature Communications* **7**, 11779 (2016).

[38] Yang, H., Boulle, O., Cros, V., Fert, A. & Chshiev, M. Controlling Dzyaloshinskii-Moriya Interaction via Chirality Dependent Layer Stacking, Insulator Capping and Electric Field. *arXiv:* 1603.01847 (2016).

[39] Johnson, M. T., Bloemen, P. J. H., Broeder, F. J. a. D. & Vries, J. J. D. Magnetic anisotropy in metallic multilayers. *Reports on Progress in Physics* **59**, 1409–1458 (1999).

[40] Nagaosa, N., Onoda, S., MacDonald, A. H. & Ong, N. P. Anomalous Hall effect. *Reviews of Modern Physics* **82**, 1539–1592 (2010).

[41] Huang, S. X. & Chien, C. L. Extended Skyrmion Phase in Epitaxial FeGe(111) Thin Films. *Physical Review Letters* **108**, 267201 (2012).

[42] Matsuno, J. *et al.* Interface-driven topological Hall effect in $SrRuO_3$-$SrIrO_3$ bilayer. *Science Advances* **2**, e1600304 (2016).

[43] Song, C.-L. *et al.* Dopant clustering, electronic inhomogeneity, and vortex pinning in iron-based superconductors. *Physical Review B* **87**, 214519 (2013).

[44] Parkin, S. S. P., Hayashi, M. & Thomas, L. Magnetic domain-wall racetrack memory. *Science* **320**, 190–194 (2008).

[45] Kang, W. *et al.* Voltage Controlled Magnetic Skyrmion Motion for Racetrack Memory. *Scientific Reports* **6**, 23164 (2016).

[46] Vansteenkiste, A. *et al.* The design and verification of MuMax3. *AIP Advances* **4**, 107133 (2014).

[47] Malozemoff, A. P. & Slonczewski, J. C. *Magnetic Domain Walls in Bubble Materials* (Academic Press, New York, 1979), 1 edn.

Acknowledgments

Author Contributions

A.S., M.T., F.E., and C.P. designed and initiated the research. M.R. deposited the films, and characterized them with A.S. M.Y.I. conducted the MTXM experiments. A.K.C.T. performed the MFM experiments and analyzed the imaging data with A.S., and P.H. validated the MFM results. M.R. and A.P.P. performed transport experiments and analyzed the data with A.S. A.L.G.O. performed micromagnetic simulations. K.H.K. and C.K.G. carried out the DFT calculations. A.S. and C.P. coordinated the project and wrote the manuscript. All authors discussed the results and provided inputs to the manuscript.

Additional Information

Further details of the results and methods are provided in Supplementary Information. Correspondence and request for materials should be addressed to A.S. and C.P.

Methods

Film Deposition. Multilayer films consisting of:

Ta(30)/Pt(100)/[Ir(10)/**Fe(0-6)/Co(4-6)**/Pt(10)]$_{20}$/Pt(20)

(layer thickness in Å in parentheses) were deposited on thermally oxidized 100 mm Si wafers by DC magnetron sputtering at RT, using a Chiron™ UHV system (base pressure: 1×10^{-8} Torr) manufactured by Bestec GmbH. The films were simultaneously deposited on Si$_3$N$_4$ membranes (thickness: 200 nm) for MTXM measurements, and the Ir/Fe/Co/Pt stack was repeated 20 times to enhance the XMCD contrast. Further deposition and characterization details are in §S1.

MTXM Experiments were performed for several Fe/Co compositions on multilayers deposited on Si$_3$N$_4$ membranes. The data were acquired in OP geometry, with the sample plane normal to the propagation direction of circularly polarized X-ray beam, using full-field MTXM at the Advanced Light Source (XM-1 BL 6.1.2). The samples were saturated OP at +250 mT, and MTXM images were acquired through hysteresis loops at the Co L$_3$ edge ($\sim$778 eV), and in some cases, at the Fe L$_3$ edge ($\sim$708 eV) over the same sample region. The spatial length scales observed at the Co and Fe edges were calibrated using standard samples, and the Fe data were corrected for a $\sim 7\%$ CCD camera magnification artifact.

MFM Experiments were performed using a NX-10 AFM/MFM manufactured by Park Systems™. All data were acquired in ambient conditions, with the MFM mounted on a vibration-isolated platform. The MFM tips used (SSS-MFMR) were $\sim$ 30 nm in diameter, with low coercivity ($\sim$ 12 mT) and ultra-low magnetic moments ($\sim$80 emu/cm^3), optimized for non-perturbative magnetic imaging with high spatial resolution. The samples were saturated OP using fields up to 0.5 T, and measurements were performed in OP fields of up to 0.2 T with a typical tip lift of 30 nm. The contrast of MFM images for $H < 0$ has been inverted for ease of comparison with MTXM images. The zero field results reported here were consistent with those obtained after AC demagnetization. Precautions were taken to eliminate tip-induced perturbations, drift, and other artifacts, and the results obtained were reproduced several times for consistency.

Magnetization, $M(H)$, of the films was determined using SQUID magnetometry, with a Quantum Design™ Magnetic Properties Measurement System (MPMS). The saturation magnetization (M_S) varied over 0.65–1.1 MA/m across our films. The effective anisotropy (K_{eff}) of the films were determined by acquiring OP and IP hysteresis loops (e.g. Fig. 2j), and are detailed in Fig. 4d.

Electrical Transport. The magnetoresistance and Hall coefficients were measured using a lock-in technique (excitation frequency: 0-300 Hz), enabling sub-nV resolution. The measurements were performed using a custom-built variable temperature insert (VTI) housed in a high-field magnet, complemented by a Quantum Design™ Physical Properties Measurement System (PPMS). The data reported here were acquired through a full hysteresis cycle, with 25 Oe steps within $\pm H_S$ after saturation at large fields (+4 T), using small current densities (as low as 10^4 A/m^2) so as to not perturb the spin textures. Importantly, the Hall data were analyzed after carefully accounting for any magnetic field offsets between magnetization (Fig. 3a) and transport (Fig. 3b) measurements. To this end, repeated field calibrations were performed on each of the instruments using reference samples.

Further procedural details of the analysis and consistency checks are provided in §S3.

Density Functional Theory Calculations. To estimate the magnetic interactions in our stacks, we performed first-principles DFT calculations using the technique employed by Yang *et al.*[20]. The multilayer stack, Ir[3]/Fe[b]/Co[a]/Pt[3] (number of atomic layers in braces), were set up in a close-packed (111) orientation and separated by a vacuum of 10 Å along the OP direction, with the IP lattice constants set to the calculated bulk Ir value (2.74 Å).

The DMI was considered only between intralayer NN atoms to a first approximation, and used to define $d^{tot} = \sum_k d^k$, i.e. the sum of DMI coefficients, d^k, for each layer[20]. Subsequently, clockwise and anti-clockwise spin spirals were constructed across a supercell using the constrained spin method. The energy difference between these two configurations was computed and scaled by a geometry and spin-spiral dependent factor to obtain d^{tot}. This was used to determine the micromagnetic DMI strength, D_{DFT}, across our magnetic films (Fig. 1c). Exchange calculations performed by first computing U_{ex} - the total energy difference between the spin spiral (averaged over clockwise and anti-clockwise spirals) and collinear spin configurations. The exchange stiffness A_{DFT} was determined by comparing this exchange energy density to the micromagnetic exchange free energy.

Further procedural details for the DFT calculations and corresponding consistency checks are in §S2.

Micromagnetic Simulations were performed using the mumax^3 software package[46], which accounts for interfacial DMI. The multilayers were modelled with a mesh size of 4×4 nm^2 over a 2×2 μm^2 area for comparison with films. The z length of the discretization mesh, L_z, was changed to match the sample's magnetic layer thickness, with the non-magnetic spacer approximated to a uniform layer. The stack configuration used (20 repeats) was consistent with experiments, and the M_S and K_{eff} values used were obtained from SQUID measurements. Meanwhile, A and D were varied over a range of likely values to estimate their magnitude by comparing the zero field domain periodicity and the field dependence of skyrmion size. MFM images were simulated for direct comparisons with experiment using the built-in functionality of mumax^3. The MFM tip magnetization was modeled as a magnetic dipole of size 20 nm, with the tip lift set to 30 nm above the surface.

For the domain periodicity simulations, the initial magnetization was randomized, and the relaxed (final) magnetization configuration ($\vec{M}(x, y, N)$) at zero field was Fourier analyzed to determine the periodicity. The average periodicity of all 20 magnetic layers, used for comparison with MFM data, was consistent with that of the top layer. Finally, the periodicity trends with varying A and D were found to be smooth and monotonic, allowing for regression analysis to accurately estimate the magnetic parameters for each stack composition.

Micromagnetic simulations were also performed with varying D and A to compare the field evolution of skyrmion size, d_{Sk}, with experiments across various sample compositions. After obtaining the zero field magnetization profile, the magnetization configuration was relaxed at progressively increasing OP magnetic fields (steps of 15–25 mT) until saturation to obtain a 'virgin' magnetization curve. The magnetization configurations obtained at each field were used to simulate the corresponding MFM images. The skyrmion size $d_{Sk}^{MFM}(H)$ was determined by averaging

over Gaussian fits to the simulated MFM profiles of several skyrmions (typically 5-10) identified from magnetization images.

Finally, simulations were performed to compare the observed size and field evolution of skyrmions with the corresponding phenomenology of bubble systems[47]. When magnetic bubbles of comparable sizes (40-100 nm) were artificially introduced in our films, they were found to be highly unstable – both at zero and finite fields – immediately transforming into chiral domain walls or skyrmions.

Determining Magnetic Parameters. The saturation magnetization, M_S, and effective anisotropy, K_{eff} (Fig. 4d), were determined from SQUID magnetometry measurements. The exchange stiffness, A_{est} (Fig. 4e), expected to vary by $\sim 15\%$ (11.0 - 12.6 pJ/m) across samples, was estimated from DFT calculations by linear interpolation of the results obtained with varying Fe/Co compositions (Fig. 1b). The corresponding DMI, D_{est} (Fig. 4f), was determined by performing a χ^2-fits to the domain periodicity at zero magnetic field in MFM experiments with micromagnetic simulations while varying D and A.

Subsequently, the validity of D_{est} and A_{est} was established independently by performing χ^2-fits to the skyrmion size, $d_{Sk}^{MFM}(H)$, between experiments and simulations for various combinations of D and A across the films (details in §S4).

The parameters shown in Fig. 4d-f were used together with Eqn. 1 to obtain κ_{est}. The evolution of skyrmion configuration with κ_{est} was analyzed using Delaunay triangulation techniques (details in §S5).

Magnetic Microscopy and Skyrmion Properties. To determine the domain periodicity, the MTXM and MFM images were analyzed in Fourier space. The position and width of the FT peak were used to quantify the domain periodicity and the error bar respectively (Fig. 2k). Meanwhile, the skyrmion sizes, d_{Sk}, were determined from MTXM and MFM measurements by performing 2D isotropic Gaussian fits to skyrmions identified within a $\sim 6 \times 6$ μm^2 field-of-view ($\sim 2 \times 2$ μm^2 for MFM simulations). The error bars for d_{Sk} represent a true spread in the observed size of multiple skyrmions in our films, consistent with reports in confined geometries[22]. The numbers for d_{Sk} reported here are raw estimates of skyrmion width – no deconvolution has been performed to account for the X-ray point spread function or beam profile, or the MFM tip size.